# Semiconductor-Nanowire-Based Superconducting Qubit

T. W. Larsen,[1] K. D. Petersson,[1] F. Kuemmeth,[1] T. S. Jespersen,[1] P. Krogstrup,[1] J. Nygård,[1,2] and C. M. Marcus[1]

[1]*Center for Quantum Devices, Niels Bohr Institute, University of Copenhagen, Copenhagen 2100, Denmark*
[2]*Nano-Science Center, Niels Bohr Institute, University of Copenhagen, Copenhagen 2100, Denmark*

We introduce a hybrid qubit based on a semiconductor nanowire with an epitaxially grown super-conductor layer. Josephson energy of the transmonlike device ("gatemon") is controlled by an electrostatic gate that depletes carriers in a semiconducting weak link region. Strong coupling to an on-chip microwave cavity and coherent qubit control via gate voltage pulses is demonstrated, yielding reasonably long relaxation times ($\sim 0.8\ \mu$s) and dephasing times ($\sim 1\ \mu$s), exceeding gate operation times by 2 orders of magnitude, in these first-generation devices. Because qubit control relies on voltages rather than fluxes, dissipation in resistive control lines is reduced, screening reduces cross talk, and the absence of flux control allows operation in a magnetic field, relevant for topological quantum information.

Superconducting qubits present a scalable solid state approach to building a quantum information processor [1]. Recent superconducting qubit experiments have demonstrated single and two-qubit gate operations with fidelities exceeding 99%, placing fault tolerant quantum computation schemes within reach [2]. While there are many different implementations of superconducting qubits [3–5], the key element is the Josephson junction (JJ), a weak link between superconducting electrodes. The JJ provides the necessary nonlinearity for nondegenerate energy level spacings, allowing the lowest two levels to define the qubit $|0\rangle$ and $|1\rangle$ states. Almost without exception, JJs for superconducting qubits are fabricated using an insulating $Al_2O_3$ tunnel barrier between superconducting electrodes [6]. Such superconductor-insulator-superconductor (SIS) junctions have a Josephson coupling energy, $E_J = \hbar I_c/2e$, where $I_c$ is the junction critical current and $e$ is the electron charge, which is fixed and determined through fabrication. Two SIS JJs are then typically arranged in a SQUID-loop geometry to create a flux-tunable effective $E_J$.

Previous work has demonstrated superconductor-normal-superconductor (SNS) JJs where the normal element is a semiconductor [7,8]. Introducing a semiconductor allows $E_J$ for a single junction to be readily tuned by an electric field that controls the carrier density of the normal region and thus the coupling of the superconductors. InAs nanowires allow for high quality field effect JJs due to the highly transparent Schottky barrier-free SN interface [9]. The recent development of InAs nanowires with epitaxially grown Al contacts yields an atomically precise SN interface and extends the paradigm of nanoscale bottom-up technology for superconducting JJ-based devices [10–12].

In this Letter, we present a superconducting transmon qubit based on a single epitaxial InAs-Al core-shell nanowire JJ element [13,14]. We demonstrate coherent operation of this semiconductor-superconductor hybrid qubit with coherence times of order 1 $\mu$s for the first generation of devices. We also show that the semiconductor JJ affords simple control of the qubit transition frequency by using an electrostatic gate to tune $E_J$. For this reason, we refer to our hybrid qubit as a gate tunable transmon, or "gatemon."
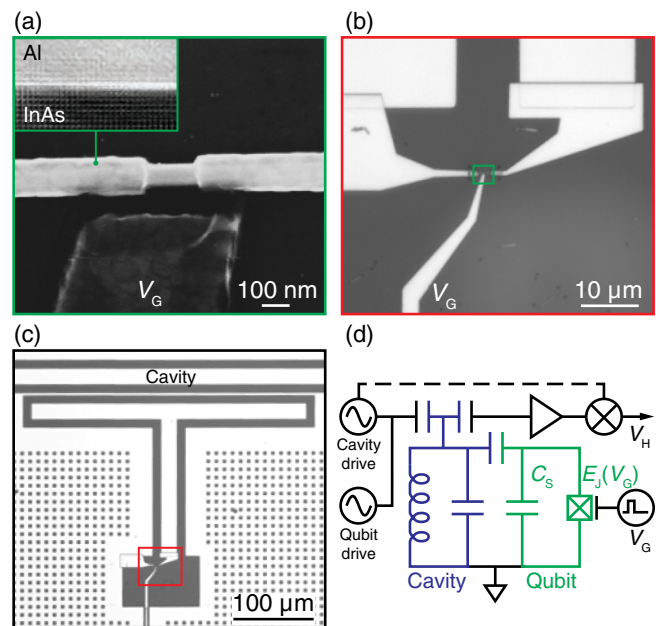


FIG. 1 (color online). InAs nanowire-based superconducting transmon qubit. (a) Scanning electron micrograph of the InAs-Al JJ. A segment of the epitaxial Al shell is etched to create a semiconducting weak link. Inset shows a transmission electron micrograph of the epitaxial InAs/Al interface. (b)–(c) Optical micrographs of the completed gatemon device. The nanowire JJ is shunted by the capacitance of the T-shaped island to the surrounding ground plane. The center pin of the coupled transmission line cavity is indicated in (c). (d) Schematic of the readout and control circuit.

Our results highlight the potential of using semiconductor materials and bottom-up fabrication techniques to form high quality JJ-based qubits that offer new means of electrical control. Independent research paralleling our own reports spectroscopic measurements on hybrid qubits using NbTiN-contacted InAs nanowires [15].

We have fabricated and measured two gatemon devices, which show similar performance. Except where noted, data are from the first device. The qubit features a single InAs SNS JJ shunted by a capacitance, $C_S$ [13,14,16]. The JJ is formed from a molecular beam epitaxy-grown InAs nanowire, $\sim$75 nm in diameter, with an *in situ* grown $\sim$30 nm thick Al shell. The Al shell forms an atomically matched SN interface leading to a proximity induced gap in the InAs core with a low density of states below the superconducting gap (hard gap) [10,11]. By wet etching away a $\sim$180 nm segment of the Al shell [Fig. 1(a)] a weak link in the superconducting shell is formed, creating the JJ [17]. A supercurrent leaking through the semiconductor core links the unetched regions and determines the Josephson coupling energy, $E_J(V_G)$, which can be tuned by changing the electron density in the semiconductor core with a nearby side gate voltage, $V_G$.

As with conventional transmons, the gatemon operates as an anharmonic LC oscillator with a nonlinear inductance provided by the JJ. The total capacitance of the gatemon qubit $C_\Sigma$ is determined by the capacitance of the T-shaped Al island to the surrounding Al ground plane, as shown in Fig. 1(c). The gatemon operates with $E_J \gg E_C$, where the charging energy, $E_C = e^2/2C_\Sigma$. In this regime, decoherence due to either low frequency charge noise on the island or quasiparticle tunneling across the JJ is strongly suppressed. For many conducting channels in the wire, the qubit transition frequency is given by $f_Q = E_{01}/h \approx \sqrt{8E_C E_J(V_G)}/h$. The difference between $E_{01}$ and the next successive levels, $E_{12}$, is the anharmonicity, $\alpha = E_{12} - E_{01} \approx -E_C$. From electrostatic simulations we estimate a charging energy of $E_C/h \approx 200$ MHz ($C_\Sigma \approx 94$ fF). With this charging energy and $E_{01}/h = 6$ GHz we get $I_c = eE_{01}^2/4E_C\hbar = 45$ nA (with an effective junction inductance of 7.3 nH), consistent with transport measurements on the same kind of NWs (not shown). From microwave spectroscopy of our gatemon we measure $\alpha/h \approx -100$ MHz. We speculate that the discrepancy between the measured anharmonicity and $-E_C$ is due to a nonsinusoidal current-phase relation for the NW JJ resulting in a reduced nonlinearity in the Josephson inductance [15].

The gatemon is coupled to a $\lambda/2$ superconducting transmission line cavity with a bare resonance frequency $f_C \approx 5.96$ GHz and quality factor, $Q \sim 1500$. The cavity is used for dispersive readout of the qubit with homodyne detection [Fig. 1(d)] [18]. Both the cavity and qubit leads are patterned by wet etching an Al film on an oxidized high resistivity Si substrate. Nanowires are transferred from the
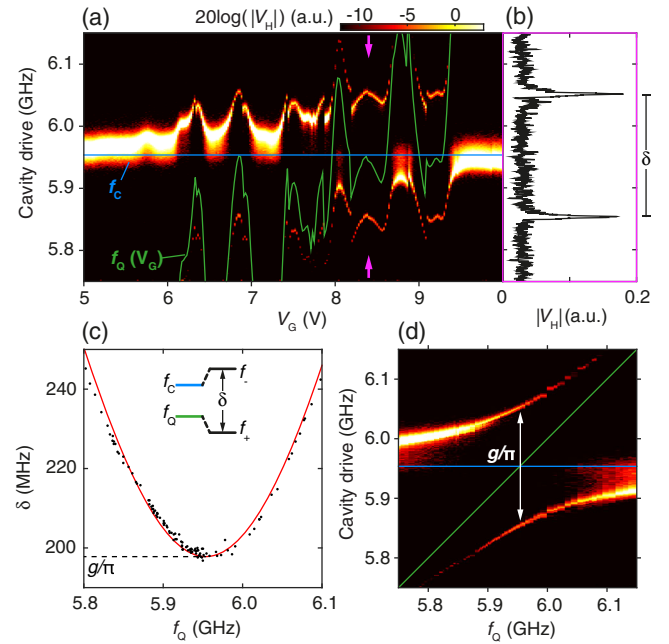


FIG. 2 (color online).   Strong coupling of the gatemon to the microwave cavity. (a) Cavity transmission as a function of the cavity drive frequency and $V_G$. The solid blue line shows the bare cavity resonance frequency $f_C$, while the solid green line indicates the gate-voltage dependent qubit frequency $f_Q(V_G)$ extracted from the data. (b) Cavity transmission as a function of the cavity drive at the position indicated by the purple arrows in (a). (c) Frequency splitting between the hybridized qubit-cavity states, $\delta$, as a function of $f_Q$, as extracted from (a). From fitting the solid theory curve we extract the qubit-cavity coupling strength, $g/2\pi = 99$ MHz. (d) Parametric plot of the data from (a) as a function of the cavity drive and qubit frequency $f_Q$.

growth substrate to the device chip using a dry deposition technique [19]. During transfer, a PMMA mask ensures nanowires are only deposited on the device inside a $85~\mu\text{m} \times 56~\mu\text{m}$ window where the JJ is fabricated. Following the nanowire shell etch, the nanowire contacts and gate are patterned from Al using a lift-off process with an ion mill step to remove the native $Al_2O_3$ prior to deposition. Measurements are performed with the sample inside an Al box mounted at the mixing chamber of a cryogen-free dilution refrigerator with a base temperature $<50$ mK [18].

Gatemon-cavity coupling was investigated by measuring cavity transmission at low drive power as a function of the cavity drive frequency and gate voltage $V_G$, with $f_Q \sim f_C$ [Fig. 2(a)]. Aperiodic fluctuations in the resonance as a function of $V_G$, with regions of widely split transmission peaks, were observed [Fig. 2(b)]. These gate-dependent, repeatable fluctuations in the cavity resonance are associated with mesoscopic fluctuations in the nanowire transmission—appearing also as fluctuations of normal-state conductance, $G_N(V_G)$ [7]—which cause fluctuations in gatemon frequency, $f_Q \propto \sqrt{I_c(V_G)}$. The changing
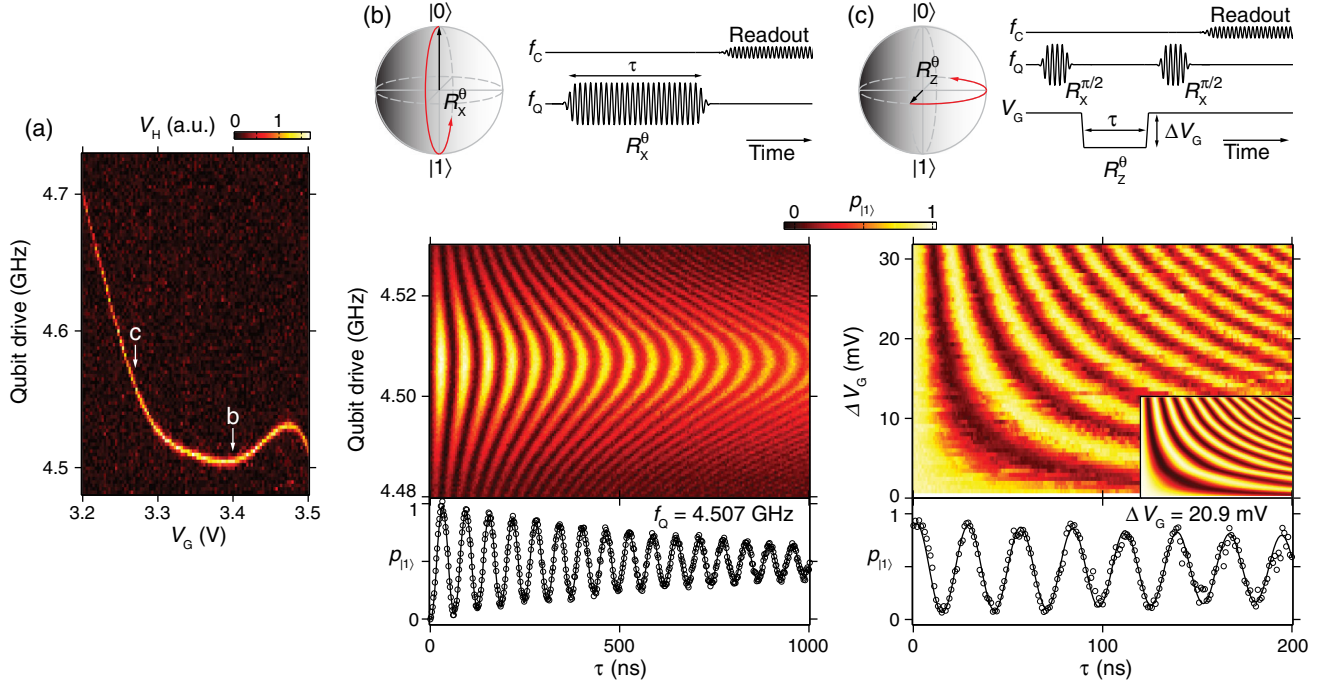
FIG. 3 (color online).   Gatemon spectroscopy and coherent control. (a) The qubit resonance frequency as a function of gate voltage $V_G$ is observed as a distinct feature. (b) Coherent Rabi oscillations are performed at point b in (a) ($V_G = 3.4$ V) by applying microwave pulse for time $\tau$ to drive the qubit followed by a readout microwave pulse to probe the cavity response. The main panel shows coherent qubit oscillations as a function of driving frequency and $\tau$. The lower panel shows coherent oscillations at the qubit resonant frequency, corresponding to rotations about the $X$ axis of the Bloch sphere. (c) Coherent oscillations about the $Z$ axis of the Bloch sphere are performed at point c in (a) ($V_G = 3.27$ V) by applying a gate voltage pulse $\Delta V_G$ to detune the qubit resonance frequency for time $\tau$. A 15 ns $R_X^{\pi/2}$ microwave pulse is first applied to rotate the qubit into the $X$-$Y$ plane of the Bloch sphere and, following the gate pulse, a second $R_X^{\pi/2}$ microwave pulse is used to rotate the qubit out of the $X$-$Y$ plane for readout. The main panel shows coherent $Z$ rotations as a function of $\Delta V_G$ and $\tau$. The main panel inset shows the simulated qubit evolution based on $\Delta f_Q(V_G)$ extracted from (a). The lower panel shows coherent $Z$ oscillations as a function of $\tau$ for $\Delta V_G = 20.9$ mV. In both (b) and (c) the demodulated cavity response $V_H$ is converted to a normalized qubit state probability $p_{|1\rangle}$ by fitting $X$ rotations to a damped sinusoid of the form $V_H^0 + \Delta V_H \exp(-\tau/T_{\text{Rabi}}) \sin(\omega\tau + \theta)$ to give $p_{|1\rangle} = (V_H - V_H^0)/2\Delta V_H + 1/2$. The solid curves in the lower panels of (b) and (c) are also fits to exponentially damped sine functions.

qubit frequency, in turn, pulls on the cavity resonance, resulting in the observed response. The split cavity peaks indicate hybridized qubit and cavity states in the strong coupling regime. The coupling strength $g$ is found to exceed the qubit and cavity decoherence rates, allowing the vacuum Rabi splitting to be resolved [20]. Writing the hybridized qubit-cavity state frequencies as $f_\pm = \left[f_Q + f_C \pm \sqrt{(f_Q - f_C)^2 + 4(g/2\pi)^2}\right]/2$, Fig. 2(c) shows the splitting $\delta = f_+ - f_-$ as a function of the qubit frequency $f_Q$. From the fit to the data we extract $g/2\pi = 99$ MHz. A parametric plot [Fig. 2(d)] of the data in Fig. 2(a), as a function of the extracted $f_Q$, reveals the avoided crossing for the hybridized qubit-cavity states [20].

Demonstrations of qubit control were performed in the dispersive regime, $|f_Q - f_C| \gg g/2\pi$. Figure 3(a) shows $f_Q$ as a function of gate voltage $V_G$ obtained by measuring the qubit-state-dependent cavity response following a

second 2 $\mu$s microwave tone. When the qubit drive was on resonance with $f_Q$, a peak in the cavity response was observed, yielding a reproducible gate voltage dependence. At a fixed gate voltage [point b in Fig. 3(a)] we measure in Fig. 3(b) the cavity response while varying the qubit drive frequency and the length of the qubit microwave pulse to observe coherent Rabi oscillations. Data in the main panel of Fig. 3(b) were acquired over several hours, highlighting the stability of the device.

While pulsed microwaves allow rotations about axes in the $X$-$Y$ plane of the Bloch sphere, rotations about the $Z$ axis may be performed by adiabatically pulsing $V_G$ to detune the qubit resonance frequency. Such dynamic control of the qubit frequency is important for fast two qubit gate operations where the resonant frequencies of two coupled qubits are brought close to each other [2,21]. Figure 3(c) shows $Z$ rotations performed by first applying an $R_X^{\pi/2}$ pulse to rotate into the $X$-$Y$ plane of the Bloch
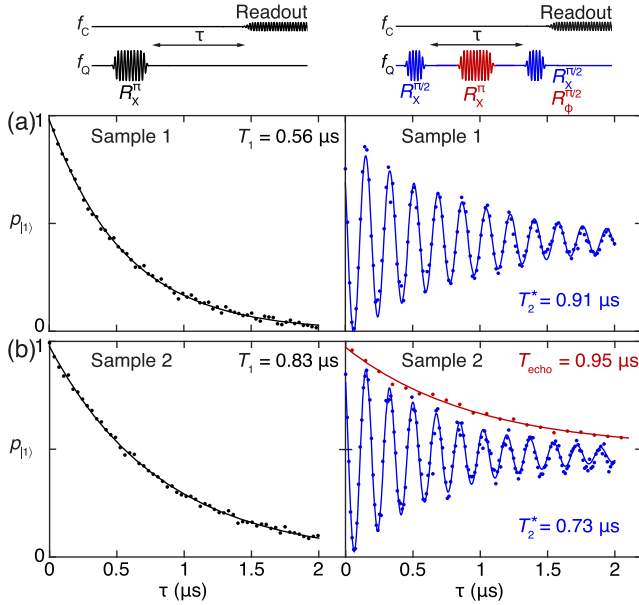
FIG. 4 (color online). Gatemon quantum coherence. (a) Left panel shows a lifetime measurement for sample 1 at point b in Fig. 3(a) ($V_G = 3.4$ V). A 30 ns $R_X^\pi$ pulse excites the qubit to the $|1\rangle$ state and we vary the wait time $\tau$ before readout. The solid line is a fit to an exponential curve. The right panel shows a Ramsey experiment used to determine $T_2^*$ for sample 1 with the wait time, $\tau$, between two slightly detuned 15 ns $R_X^{\pi/2}$ pulses varied before readout. The solid curve is a fit to an exponentially damped sinusoid. (b) We repeat the lifetime and Ramsey experiments as in (a) for sample 2 with $f_Q = 4.426$ GHz ($V_G = -11.3$ V). In red, we perform a Hahn echo experiment by inserting an $R_X^\pi$ pulse between two $R_X^{\pi/2}$ pulses. The decay envelope is measured by varying the phase $\phi$ of the second $\pi/2$ microwave pulse and extracting the amplitude of the oscillations. The solid red line is a fit to an exponential curve.

sphere followed by a negative voltage pulse $\Delta V_G$, which causes the qubit state to precess about the $Z$ axis at the difference frequency, $\Delta f_Q = f_Q(V_G - \Delta V_G) - f_Q(V_G)$. Finally, a second $R_X^{\pi/2}$ pulse was applied to rotate the qubit out of the $X$-$Y$ plane and measure the resulting qubit state. The observed precession frequency is consistent with the $\Delta f_Q$ predicted from the spectroscopy data in Fig. 3(a) [Fig. 3(c) main panel inset].

Gatemon coherence times were measured quantitatively in both devices [Fig. 4]. The relaxation time $T_1$ was measured by initializing the qubit to $|1\rangle$ and varying the waiting time $\tau$ before readout, giving $T_1 = 0.56$ $\mu$s for the first device, measured at operating point b in Fig. 3(a). The decay envelope of a Ramsey measurement [Fig. 4(a), right panel] gives a dephasing time, $T_2^* = 0.91$ $\mu$s at the same operating point. Noting that $T_2^* \approx 2T_1$, we conclude that at this operating point, coherence was limited by energy relaxation. Figure 4(b) shows coherence times for the second sample, showing a slightly longer relaxation

time, $T_1 = 0.83$ $\mu$s [Fig. 4(b), left panel]. In this device, inhomogeneous dephasing time was shorter, $T_2^* = 0.73$ $\mu$s. In Fig. 4(b) right panel (in red) we show that applying a Hahn echo pulse sequence, which effectively cancels low frequency noise in $f_Q$, increases the dephasing time to $T_{\text{echo}} = 0.95$ $\mu$s. This indicates a greater degree of low frequency noise in $E_J(V_G)$ in the second device. The observation that $T_{\text{echo}}$ does not reach $2T_1$ indicates that higher frequency noise fluctuations faster than $\tau$ also contributes to dephasing.

Coherence times for these first-generation gatemon devices are comparable to SIS transmons reported a few years ago, where typically $T_2^* \sim T_1 \sim 2$ $\mu$s [22]. Longer coherence times, $T_2^* \sim 15$ and $T_1 \sim 40$ $\mu$s, have since been reported for planar flux-tunable SIS transmon devices through careful optimization [16]. Following these developments, we anticipate that our gatemon relaxation times can be substantially improved by removing the $SiO_2$ dielectric layer [23] and more careful sample processing to reduce interface losses in the capacitor [24], along with increased magnetic and infrared radiation shielding [25,26]. This should in turn extend dephasing times and allow for the low frequency noise spectrum to be characterized using dynamical decoupling [3]. Electrical noise coupling to $E_J(V_G)$ due to charge traps at the nanowire surface, along with disorder-induced fluctuations in $E_J(V_G)$, could potentially be reduced through InAs surface passivation [27].

Frequency control of conventional flux-tunable SIS transmons is typically achieved using on-chip superconducting current loops. The large (mA scale) currents used to control flux-tunable transmons makes scaling to many qubits difficult using control electronics that pass into the cryogenic environment through normal coax lines, filters, and attenuators. On-chip voltage pulses are relatively easily screened, compared to flux pulses, which will reduce cross talk between qubit control lines. Gatemons, with voltage tunable $f_Q$, also offer new possibilities for large scale superconducting architectures. For instance, FET-based cryogenic multiplexers [28,29] have recently been developed for millikelvin temperatures and would be well suited to gate control of large multi-gatemon circuits.

Finally, we note that the epitaxial InAs-Al nanowires are expected to support Majorana bound states [30,31] due to the strong spin-orbit coupling and large $g$ factor ($\sim$10) of InAs. Recent theoretical work has proposed using transmons to manipulate and probe topologically protected qubits built from Majorana bound states [32,33]. The absence of flux control may particularly suit gatemons for operation in magnetic fields required for Majorana bound states, allowing InAs nanowire-based gatemons to be readily coupled to topological qubits made using the same material technology.

———————

[1] M. H. Devoret and R. J. Schoelkopf, Science **339**, 1169 (2013).

[2] R. Barends, J. Kelly, A. Megrant, A. Veitia, D. Sank, E. Jeffrey, T. C. White, J. Mutus, A. G. Fowler, B. Campbell, Y. Chen, Z. Chen, B. Chiaro, A. Dunsworth, C. Neill, P. O'Malley, P. Roushan, A. Vainsencher, J. Wenner, A. N. Korotkov, A. N. Cleland, and J. M. Martinis, Nature (London) **508**, 500 (2014).

[3] J. Bylander, S. Gustavsson, F. Yan, F. Yoshihara, K. Harrabi, G. Fitch, D. G. Cory, Y. Nakamura, J.-S. Tsai, and W. D. Oliver, Nat. Phys. **7**, 565 (2011).

[4] Z. Kim, B. Suri, V. Zaretskey, S. Novikov, K. D. Osborn, A. Mizel, F. C. Wellstood, and B. S. Palmer, Phys. Rev. Lett. **106**, 120501 (2011).

[5] V. E. Manucharyan, N. A. Masluk, A. Kamal, J. Koch, L. I. Glazman, and M. H. Devoret, Phys. Rev. B **85**, 024521 (2012).

[6] H. Paik, D. I. Schuster, L. S. Bishop, G. Kirchmair, G. Catelani, A. P. Sears, B. R. Johnson, M. J. Reagor, L. Frunzio, L. I. Glazman, S. M. Girvin, M. H. Devoret, and R. J. Schoelkopf, Phys. Rev. Lett. **107**, 240501 (2011).

[7] Y. J. Doh, J. A. van Dam, A. L. Roest, E. P. A. M. Bakkers, L. P. Kouwenhoven, and S. De Franceschi, Science **309**, 272 (2005).

[8] S. Abay, D. Persson, H. Nilsson, F. Wu, H. Q. Xu, M. Fogelström, V. Shumeiko, and P. Delsing, Phys. Rev. B **89**, 214508 (2014).

[9] M. Ebel and C. Busch and U. Merkt and M. Grajcar and T. Plecenik and E. Il'ichev, Phys. Rev. B **71**, 052506 (2005).

[10] P. Krogstrup, N. L. B. Ziino, S. M. Albrecht, M. H. Madsen, E. Johnson, J. Nygård, C. M. Marcus, and T. S. Jespersen, Nat. Mater. **14**, 400 (2015).

[11] W. Chang, S. M. Albrecht, T. S. Jespersen, F. Kuemmeth, P. Krogstrup, J. Nygård, and C. M. Marcus, Nat. Nanotechnol. **10**, 232 (2015).

[12] Y.-P. Shim and C. Tahan, Nat. Commun. **5**, 4225 (2014).

[13] J. Koch, T. M. Yu, J. Gambetta, A. A. Houck, D. I. Schuster, J. Majer, A. Blais, M. H. Devoret, S. M. Girvin, and R. J. Schoelkopf, Phys. Rev. A **76**, 042319 (2007).

[14] A. A. Houck, D. I. Schuster, J. M. Gambetta, J. A. Schreier, B. R. Johnson, J. M. Chow, L. Frunzio, J. Majer, M. H. Devoret, S. M. Girvin, and R. J. Schoelkopf, Nature (London) **449**, 328 (2007).

[15] G. de Lange, B. van Heck, A. Brunol, D. J. van Woerkom, A. Geresdil, S. R. Plissard, E. P. A. M. Bakkers, A. R. Akhmerov, and L. DiCarlo, following Letter, Phys. Rev. Lett. **115**, 127002 (2015).

[16] R. Barends, J. Kelly, A. Megrant, D. Sank, E. Jeffrey, Y. Chen, Y. Yin, B. Chiaro, J. Mutus, C. Neill, P. O'Malley, P. Roushan, J. Wenner, T. C. White, A. N. Cleland, and J. M. Martinis, Phys. Rev. Lett. **111**, 080502 (2013).

[17] The nanowire aluminum shell is etched using a PMMA mask defined by e-beam lithography. We etch for 12 s in 50 °C Transene Aluminum Etchant Type D followed directly by 30 s in room temperature DI water and a 10 s IPA rinse.

[18] See Supplemental Material at http://link.aps.org/supplemental/10.1103/PhysRevLett.115.127001 for further details of the experimental setup.

[19] W. Chang, Ph.D. thesis, Harvard University, Cambridge, MA, 2014.

[20] A. Wallraff, D. I. Schuster, A. Blais, L. Frunzio, R.-S. Huang, J. Majer, S. Kumar, S. M. Girvin, and R. J. Schoelkopf, Nature (London) **431**, 162 (2004).

[21] L. DiCarlo, J. M. Chow, J. M. Gambetta, L. S. Bishop, B. R. Johnson, D. I. Schuster, J. Majer, A. Blais, L. Frunzio, S. M. Girvin, and R. J. Schoelkopf, Nature (London) **460**, 240 (2009).

[22] A. A. Houck, J. A. Schreier, B. R. Johnson, J. M. Chow, J. Koch, J. M. Gambetta, D. I. Schuster, L. Frunzio, M. H. Devoret, S. M. Girvin, and R. J. Schoelkopf, Phys. Rev. Lett. **101**, 080502 (2008).

[23] A. D. O'Connell, M. Ansmann, R. C. Bialczak, M. Hofheinz, N. Katz, E. Lucero, C. McKenney, M. Neeley, H. Wang, E. M. Weig, A. N. Cleland, and J. M. Martinis, Appl. Phys. Lett. **92**, 112903 (2008).

[24] C. M. Quintana, A. Megrant, Z. Chen, A. Dunsworth, B. Chiaro, R. Barends, B. Campbell, Y. Chen, I. C. Hoi, E. Jeffrey, J. Kelly, J. Y. Mutus, P. J. J. O'Malley, C. Neill, P. Roushan, D. Sank, A. Vainsencher, J. Wenner, T. C. White, A. N. Cleland, and J. M. Martinis, Appl. Phys. Lett. **105**, 062601 (2014).

[25] A. D. Córcoles, J. M. Chow, J. M. Gambetta, C. Rigetti, J. R. Rozen, G. A. Keefe, M. B. Rothwell, M. B. Ketchen, and M. Steffen, Appl. Phys. Lett. **99**, 181906 (2011).

[26] R. Barends, J. Wenner, M. Lenander, Y. Chen, R. C. Bialczak, J. Kelly, E. Lucero, P. O'Malley, M. Mariantoni, D. Sank, H. Wang, T. C. White, Y. Yin, J. Zhao, A. N. Cleland, J. M. Martinis, and J. J. A. Baselmans, Appl. Phys. Lett. **99**, 113507 (2011).

[27] A. C. Ford, S. B. Kumar, R. Kapadia, J. Guo, and A. Javey, Nano Lett. **12**, 1340 (2012).

[28] D. R. Ward, D. E. Savage, M. G. Lagally, S. N. Coppersmith, and M. A. Eriksson, Appl. Phys. Lett. **102**, 213107 (2013).

[29] H. Al-Taie, L. W. Smith, B. Xu, P. See, J. P. Griffiths, H. E. Beere, G. A. C. Jones, D. A. Ritchie, M. J. Kelly, and C. G. Smith, Appl. Phys. Lett. **102**, 243102 (2013).

[30] V. Mourik, K. Zuo, S. M. Frolov, S. R. Plissard, E. P. A. M. Bakkers, and L. P. Kouwenhoven, Science **336**, 1003 (2012).

[31] A. Das, Y. Ronen, Y. Most, Y. Oreg, M. Heiblum, and H. Shtrikman, Nat. Phys. **8**, 887 (2012).

[32] F. Hassler, A. R. Akhmerov, and C. W. J. Beenakker, New J. Phys. **13**, 095004 (2011).

[33] E. Ginossar and E. Grosfeld, Nat. Commun. **5**, 4772 (2014).